LASER & PHOTONICS REVIEWS
www.lpr-journal.org

Difference Frequency Generation from AA-Stacked WS_2 Coupled with Dual-Resonant Au Nanocavity

Chao Guan, Xiaobo Han, Kai Wang, Yuda Wan, Liyu Zhang, Jiaxing Yang, Shuzheng Chen, Zhongao Huang, Hua Long, and Peixiang Lu**

Difference frequency generation (DFG), underlying on second-order nonlinear optical effect, is a parametric down-conversion process that is widely used to generate and amplify broadband signals. It leads to the wide applications in tunable laser systems and infrared sources, as well as quantum light sources. However, it is still challenging to realize the widely tunable, ultra-compact, and efficient DFG light sources in nanoscales. Here, a boosting DFG from AA-stacked WS_2 coupled with a tunable dual-resonant nanocavity, which is composed of Au nanodisk arrays and TiO_2/Au film, is experimentally demonstrated. In this nanocavity, the Fabry-Perot mode and localized surface plasmon resonance mode can be independently tuned to match well with the pump (515 nm) and the signal (750–900 nm) wavelength in DFG, respectively. Over two order-of-magnitude enhancement of DFG is successfully achieved ranging from 1200 to 1650 nm (e.g., 812× at 1445 nm). This work proposes a dual-resonance hybrid nanocavity and shines the way to the DFG enhancement in transitional metal dichalcogenides, expanding the prospects in subwavelength coherent light sources and other optoelectronic devices.

1. Introduction

Nonlinear optics form the foundation of diverse optical applications from data storage to lithography and high-resolution microscopy.[1–3] Parametric nonlinear process as the core of nonlinear optics, including optical parametric up-conversion and down-conversion, can provide tunable coherent light sources in a wide spectral range.[4,5] Difference frequency generation (DFG) serves as the fundamental principle underlying several crucial optical parametric down-conversion processes, including spontaneous parametric down-conversion (SPDC),[6,7] terahertz (THz) emission,[8,9] and optical parametric generation (OPG), amplification (OPA), oscillation (OPO). To be specific, the SPDC has been used to create a vast variety of photonic quantum states, including single[10] and entangled photons,[11] squeezed states,[12] and cluster states,[13–15] which currently constitute the building block for entangled photon pair generation in quantum optics. THz science and technology have promising application prospects in various fields such as spectroscopy, wireless communication, security imaging, and sensing. While OPG, OPA, and OPO, play an important role in ultrafast spectroscopy, tunable narrow-band laser sources, as well as entangled photon generation[16–19] and revolutionizes modern-day laser technology and constitutes a vital key element for photonic quantum technology.[17] In 1965, DFG was first discovered in ADP crystal.[20] Presently, nonlinear birefringent crystals continue to be predominant in DFG.[21] Nevertheless, momentum conservation requires a specific dispersion relationship,[22–24] limiting the bandwidths. Moreover, nonlinear bulk crystals require a rigorous value of incident angle for phase match conditions, hindering the potential applications in large-scale on-chip integration. Therefore, the study on nanoscale and multifunctional OPA devices can undoubtedly pave the way for advanced technological applications.

In the past few years, layered materials have drawn lots of study interest, such as graphene, black phosphorus, and transition metal dichalcogenides (TMDs).[25–30] In particular, monolayer TMDs possess a large second-order susceptibility ($\chi^{(2)}$) due to inversion symmetry breaking,[31,32] providing an ideal platform for giant nonlinear optical response at room temperature.[33] Moreover, the nonlinear frequency conversion process is compressed to single atomic thickness in monolayer TMDs, which relaxes the phase-matching constraints and thus offers practically unlimited bandwidth for parametric nonlinear processes.[34,35] However, compared with bulk materials, TMDs in 2D form have much shorter light-matter interaction lengths, which inherently limits frequency conversion efficiency. Therefore, many previous reports have focused on the enhancement of the parametric up-conversion interactions in monolayer TMDs, such as sec-

C. Guan, K. Wang, Y. Wan, L. Zhang, J. Yang, S. Chen, Z. Huang, H. Long, P. Lu
Wuhan National Laboratory for Optoelectronics and School of Physics
Huazhong University of Science and Technology
Wuhan430074, China
E-mail: kale_wong@hust.edu.cn; lupeixiang@hust.edu.cn
X. Han, P. Lu
Hubei Key Laboratory of Optical Information and Pattern Recognition
Wuhan Institute of Technology
Wuhan430205, China
K. Wang
School of Electronic and Information Engineering
Hubei University of Science and Technology
Xianning437100, China
The ORCID identification number(s) for the author(s) of this article can be found under https://doi.org/10.1002/lpor.202401895

DOI: 10.1002/lpor.202401895

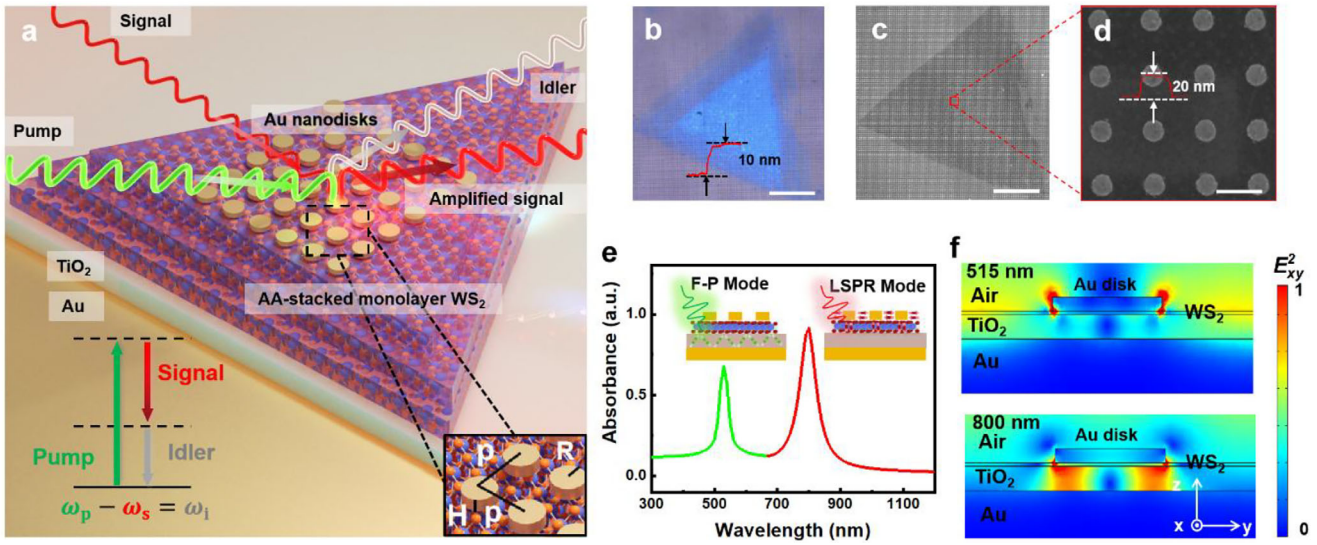

Figure 1. a) Schematic illustration of AA-stacked monolayer WS_2 sandwiched between Au nanodisks and TiO_2 film. The 60 nm Au film is covered by TiO_2 film with a thickness (*T*) of 40 nm. AA-stacked 6 layers WS_2 on the TiO_2 film. The Au nanoarray period (*P*) is 220 nm, radius (*R*) is 50 nm, and height (*H*) is 20 nm. b) Optical microscope image of hybrid nanocavity. The total thickness of AA-stacked 6 layers WS_2 is ≈10 nm. c) Corresponding SEM image of hybrid nanocavity. d) Enlarged SEM image of the region is outlined in the square of Figure 1c. The height of the Au nanodisk is ≈20 nm. The scale bars are 10 μm (b and c) and 200 nm (d), respectively. e) Simulated absorption spectra of the hybrid nanocavity. The F-P mode (green curve) is influenced by the TiO_2 thickness, whereas the LSPR mode (red curve) is influenced by the radius of nanodisks. f) Simulated distribution patterns of the in-plane electric field intensity (E^2_{xy}) of the pump (top) and signal (bottom) in the cross-section of the samples.

ond harmonic generation (SHG),[36–40] sum frequency generation (SFG)[41–43] and third harmonic generation,[44–46] four-wave-mixing.[47,48] Specifically, various strategies have been reported to achieve SHG enhancement, including microcavity,[49–51] plasmonic nanostructures,[52–55] dielectric metasurfaces[56,57] and exciton-polaritons,[58,59] while less attention is attached to the enhancement of parametric down-conversion processes. Recently, researchers have begun to associate different kinds of bare monolayer TMDs with DFG demonstrations[60,61] and successfully realized that valley polarization triggered the parametric process by combining a monolayer WS_2 with microcavity.[62] In addition to TMDs, silicon nitride (Si_3N_4) waveguides integrate 2D layered graphene oxide films as a promising nonlinear optical material that enhances the OPA performance of on-chip photonic integrated devices.[63] However, to develop new types of nanoscale amplifiers, efficient DFG enhancement remains the major obstacle. Enlightened by the SHG enhancement mechanism, the strong local-field effect of resonant modes in the nanocavity provides a promising approach to confine light at the subwavelength scale. Therefore, there is great potential to boost the conversion efficiency of DFG light nanosources.

In this work, we propose and experimentally demonstrate an Au nanodisks/AA-stacked WS_2/TiO_2/Au film hybrid nanocavity for the efficient DFG light nanosource. This nanocavity supports the dual resonance modes of Fabry-Perot (F-P) mode and localized surface plasmon resonance (LSPR) mode, which can be tuned to match well with the pump (515 nm) and the signal wavelength (750–900 nm) in DFG respectively. Further, the generated idler field can be coherently superimposed within AA-stacked WS_2. Successfully, over two orders of magnitudes of DFG enhancement is achieved in a broadband from 1200 to 1650 nm (e.g., 812× at 1445 nm). Moreover, the enhancement effect is independent from relative angles between pump and signal polarizations. Remarkably, we propose a hybrid nanocavity that not only provides a good platform for light-matter interactions, but also provides new inspiration for the design of efficient 2D all-optical amplifiers, on-chip frequency converters, and integrated nanoscale sources of quantum entangled photons.

DFG is a second-order nonlinear optical process that broadens the band of coherent light sources. Specifically, a high-energy pump photon (frequency ω_p) is stimulated by a tunable signal photon (frequency ω_s) to annihilate into a pair of signal and idler photons (frequency $\omega_i = \omega_p - \omega_s$), and signal photons can be seen as amplified. Therefore, the idler is the fingerprint of the DFG process in background-free detection. Moreover, amplified signal photons can be extracted from a large number of the uncoupled signal photons by the polarization-dependent DFG measurement, and according to the ratio of amplified signal photons to background signal photons, the conversion efficiency of DFG can be accurately estimated. (see Supplement S1 and Section S1, Supporting Information for more details).

To realize a highly efficient DFG nanosource, a hybrid dual-resonant nanocavity is designed as shown in **Figure 1a**. Specifically, the hybrid nanocavity is composed of Au nanodisk arrays and TiO_2/Au film, with AA-stacked WS_2 inserted as the source. AA-stacked means several monolayers with interlayer ~0°crystal angle alignment, preserving the broken inversion symmetry ($\chi^{(2)} \neq 0$). The individual Au nanodisk features radius *R*, and height *H*, arranged with the period *P*. Figure 1b shows a typical optical microscope image of the hybrid nanocavity consisting of AA-stacked 6 monolayers WS_2 (~10 nm thickness) sandwiched between Au nanodisk arrays and TiO_2/Au film (see Atomic Force Microscope (AFM) image in Supplement S1 and Figure S2a, Supporting Information). Each layer WS_2 is shaped

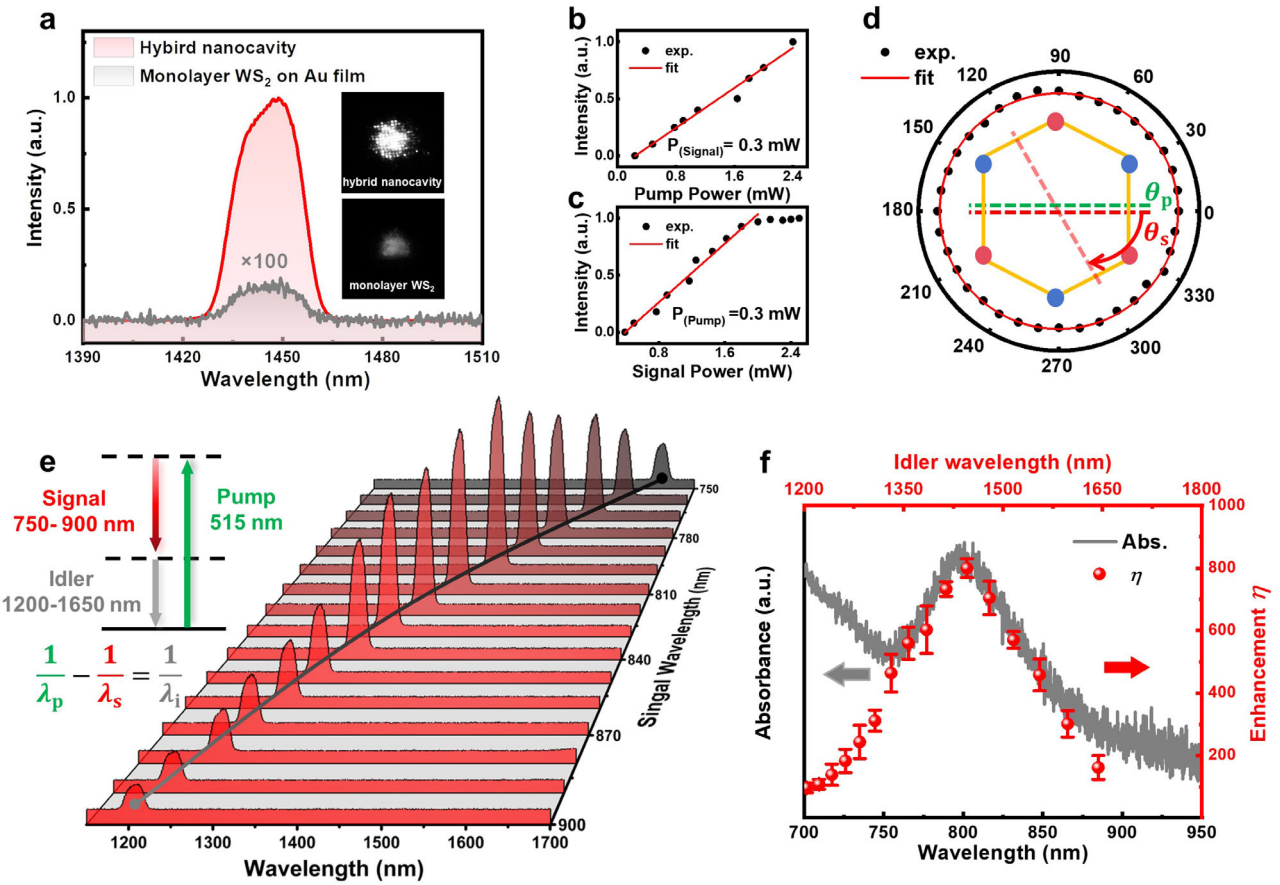

Figure 2. a) Normalized idler spectra of hybrid nanocavity (red curve) and monolayer WS_2 on Au film (gray curve). Both of the peaks are centered at 1445 nm. Inset: optical image of idler on hybrid nanocavity (top) and monolayer WS_2 on Au film (bottom) at the same excitation power. b) Normalized idler power is a linear function of the pump power with the signal power fixed at 0.3 mW. c) Normalized idler power is a linear function of the signal power with the pump power fixed at 0.3 mW. d) Relationship between the intensity of the idler and the polarization angles of the pump and signal. e) Normalized tunable idler spectra measured on hybrid nanocavity at the signal wavelength from 750 to 900 nm, and the pump wavelength fixed at 515 nm. f) Enhancement factor η (red balls) with error bars under varied signal excitation wavelengths from 750 to 900 nm. The gray line is the absorption spectra of the Au nanodisks from 700 to 950 nm.

like a triangle, with a side length of ~50 μm. Due to interference and absorption, the stacked WS_2 appears blue. The darker color indicates more layers. Thus, the uniform color of the stacked 6 layers WS_2 indicates that a high-quality sample has been prepared. The corresponding scanning electron microscopy (SEM) image is shown in Figure 1c. Note that the densely packed white dots in the image are Au nanodisk arrays. The enlarged SEM image (square marked) in Figure 1d clearly shows the arranged nanodisks, and the inset shows the ~20-nm height nanodisk measured by atomic force microscopy (see AFM image in Supplement S1 and Figure S2b, Supporting Information).

In Figure 1e, the finite-element simulation (Comsol Multiphysics) shows the absorption spectrum of the well-designed double-resonant nanocavity with typical values of $H = 20$ nm, $R = 50$ nm, $P = 220$ nm, and T (TiO_2 thickness) = 40 nm, exhibiting two distinct peaks at 515 and 800 nm. The unique nanodisk-on-mirror nanocavity configuration enables a class of hybrid modes that are strongly confined in the dielectric TiO_2, known as the F-P mode (515 nm, green line). Another resonant mode mainly from Au nanodisk arrays is known as LSPR mode (800 nm, red line). Thus, the two modes can be tuned independently due to the different physical mechanisms, which are very suitable for multi-optical parametric conversion processes, such as SFG or DFG. In detail, the identification for the origins of these two modes can be seen in Supplement S1 and Section S3 (Supporting Information). Figure 1f shows the calculated in-plane electric field distribution (E^2_{xy}) along the z-y plane of the two modes in the hybrid nanocavity. It confirms the local field enhancement both at the pump and signal wavelength. It is worth mentioning that E^2_{xy} is dominant in both resonance modes, which is very suitable for matching the polarization direction of monolayer TMDs.

To experimentally determine the DFG enhancement in the hybrid nanocavity, we measure the idler as a distinctive signature of the DFG, because of its frequency difference from the pump and signal. **Figure** 2a shows the idler spectra from the hybrid nanocavity compared with that from monolayer WS_2 on the Au film, under the pump at 515 nm and the signal at 800 nm. Remarkably, the idler intensity of the hybrid nanocavity (red shade) is much stronger than that of monolayer WS_2 (gray shade). Note that the idler spectra of monolayer WS_2 have been magnified 100×. Specifically, it indicates an 812× DFG enhancement. Insets show the optical image of idler intensity measured at the

same condition. In addition, an estimation of DFG conversion efficiency is up to $\sim 1 \times 10^{-3}$ at 1445 nm, which the conversion efficiency is the optimal result in the recent related literature (see Supplement S1 and Section S1, Supporting Information for more details). And the effective second-order nonlinear susceptibility $\chi^{(2)}_{\text{eff}}$ of ~8.851 nm V^{-1}, which is comparable to the reported values for WS_2 in earlier reports[55,64] (see Supplement S1 and Section S4, Supporting Information for more details). In addition to the observed nonlinear optics in addition to DFG, there are SHG and FWM in the hybrid nanocavity. (see Supplement S1 and Section S5, Supporting Information for more details) When the signal (or pump) power keep constant at 0.3 mW, the idler intensity I_i shows a linear variation with the pump (or signal) power, as shown in Figure 2b,c. The slope of the fitted lines is approximately ~1.0, as is expected from the theoretical Equation (1):[65]

$$P^{(2)}\left(\omega_p - \omega_s\right) = 2\varepsilon_0 \chi^{(2)}\left(\omega_p - \omega_s\right) E_p E_s \tag{1}$$

where E_i, E_p and E_s stand for the idler, the pump, and the signal electric fields, respectively. Note that the idler intensity saturates in Figure 2c when the signal power exceeds 2 mW. It could be attributed to the unbalanced photons of two input beams. Since the photon energy of the pump and signal is larger and lower than the bandgap of the WS_2 respectively, it leads to a stronger absorption of the pump compared to the signal, thus limiting the interaction efficiency.[60] Hence, it is necessary to properly match the power ratio of the signal and the pump to ensure that the intensity of the idler increases linearly with the signal or pump power. Figure 2d shows the normalized idler intensity as a function of the pump − signal polarization angle ($\theta_p - \theta_s$) measured from the hybrid nanocavity.The black dots represent experimental data, while the red curve represents the fitting result. It indicates that the idler intensity is independent of the relative angle between the pump and signal polarization directions.[61] This is because both the Au nanodisks and AA-stacked WS_2 belong to the centrosymmetric nanostructures, the polarization angle between the signal and pump does not affect the idler intensity (see more details of polarization characteristics in Supplement S1 and Section S6, Supporting Information). The polarization-independent characteristic of the hybrid nanocavity improves its general applicability and enhances the robustness.

As the inset of Figure 2e illustrates, energy and momentum conservations constrain the DFG, where pump photons annihilate, producing signal photon and idler photon pairs. From the equation $\omega = 2\pi c/\lambda$, we can obtain the relationship among wavelengths of the pump, signal, and idler. As well known, the most representative process of DFG is to generate tuned light sources. Thus, Figure 2e depicts the tuned idler spectra ranging from 1200 to 1650 nm in the hybrid nanocavity with the pump wavelength at 515 nm and the signal wavelength from 750 to 900 nm. The spectral window is exclusively modulated by the tunability of the signal beam. It is worth noting that the cavity-enhanced idler has a theoretically boundless tuning wavelength range, but the measuring of the more infrarem idler is limited by the detection equipment. Figure 2f shows the detailed enhancement factor (η) of idler intensity (red dots), together with the measured absorption spectrum of the nanocavity (gray curve), and the wavelength of the signal excitation (lower horizontal coordinate) corresponds to that of the idler (upper horizontal coordinate). The η increases first and then decreases, consisting with the trend of absorption spectrum. We found that the largest the η is obtained when the signal wavelength is matched with the peak of the LSPR mode of the nanodisk at 800 nm. It is attributed to the fact that the hybrid nanocavity shows the strongest local field at 800 nm. And the largest $\eta = 812$ is obtained at idler at 1445 nm and signal at 800 nm in agreement with the absorption peak position of Au nanodisks. It is worth noting the absorption spectrum of Au nanodisks (700–750 nm) is affected by higher resonance modes, leading the deviation in this wavelength region. When the excitation wavelength moves to 700 nm, the η decreases to ~100. It indicates that the η is very sensitive to the spectra overlap between absorption and signal spectrum, and the more excitation signal absorbed by the nanocavity, the stronger the resonance effect will be in nanocavity. It is notable that the idler intensity can be boosted by more than two orders of magnitude in such a wide range. Therefore, the hybrid nanocavity can work over a broad wavelength range with a remarkable enhancement effect. It is worth emphasizing that excellent performance characteristic endows the hybrid nanocavity with great potential in tunable sources of radiation and spectroscopy fields.

To further verify the DFG enhancement mechanisms, we systematically studied the idler spectra in different hybrid nanocavities which vary in the layer number of WS_2, TiO_2 thickness, and the parameters of the Au nanodisk array. First, the use of AA-stacked WS_2 makes a great contribution to the enhancement. As the schematic shown in the inset of **Figure 3a**, AA-stacked WS_2 means the armchair of each stacked layer in the same direction (the stacked angle $\theta = 0°$). Figure 3a shows the idler spectra from different stacked layers (n) of WS_2 on the TiO_2/Au film (absorption and Raman spectra of AA-stacked WS_2 see Supplement S1 and Section S7, Supporting Information). Obviously, the idler intensity presents an enhancement trend with increasing the layer number. Figure 3b shows the extracted idler intensity (black dots) as a function of the layer number, and the fitted slope (red line) is ~1.92, which is consistent with the theory of coherent superposition. In addition to WS_2, the idler coherent superposition enhancement of other TMDs with similar crystal structure and symmetry breaking also follows to this principle. We have performed a proof-of-principle demonstration of this concept for 1–2 layers of manually AA-stacked WSe_2, as shown in Supplement S1 and Section S8 (Supporting Information). The detailed derivation of the idler intensity from the individual layers by coherent superposition is shown below. In the inset of Figure 3b, when codirectional electric fields of the pump $\vec{E}_p$ and signal $\vec{E}_s$ make an angle of φ_k concerning the armchair direction of layer k, the generated idler electric field $\vec{E}_k$ from layer k is then $3\varphi_k$ away from the polarization of pump and signal. The total idler electric field $\vec{E}_{\text{idler}}$ can be expressed as:

$$\vec{E}_{\text{idler}} = \sum_{k=1}^{n} \vec{E}_k \tag{2}$$

According to the theory of coherent superposition, the total idler intensity I_{idler} in the stacked region can be expressed as:[66]

$$I_{\text{idler}} \propto \left|\sum_{k=1}^{n} \vec{E}_k\right|^2 = \sum_{l=1}^{n}\sum_{m=1}^{n} \vec{E}_l \cdot \vec{E}_m = \sum_{l=1}^{n}\sum_{m=1}^{n} \left|\vec{E}_l\right|\left|\vec{E}_m\right| \cos\theta_{lm} \tag{3}$$

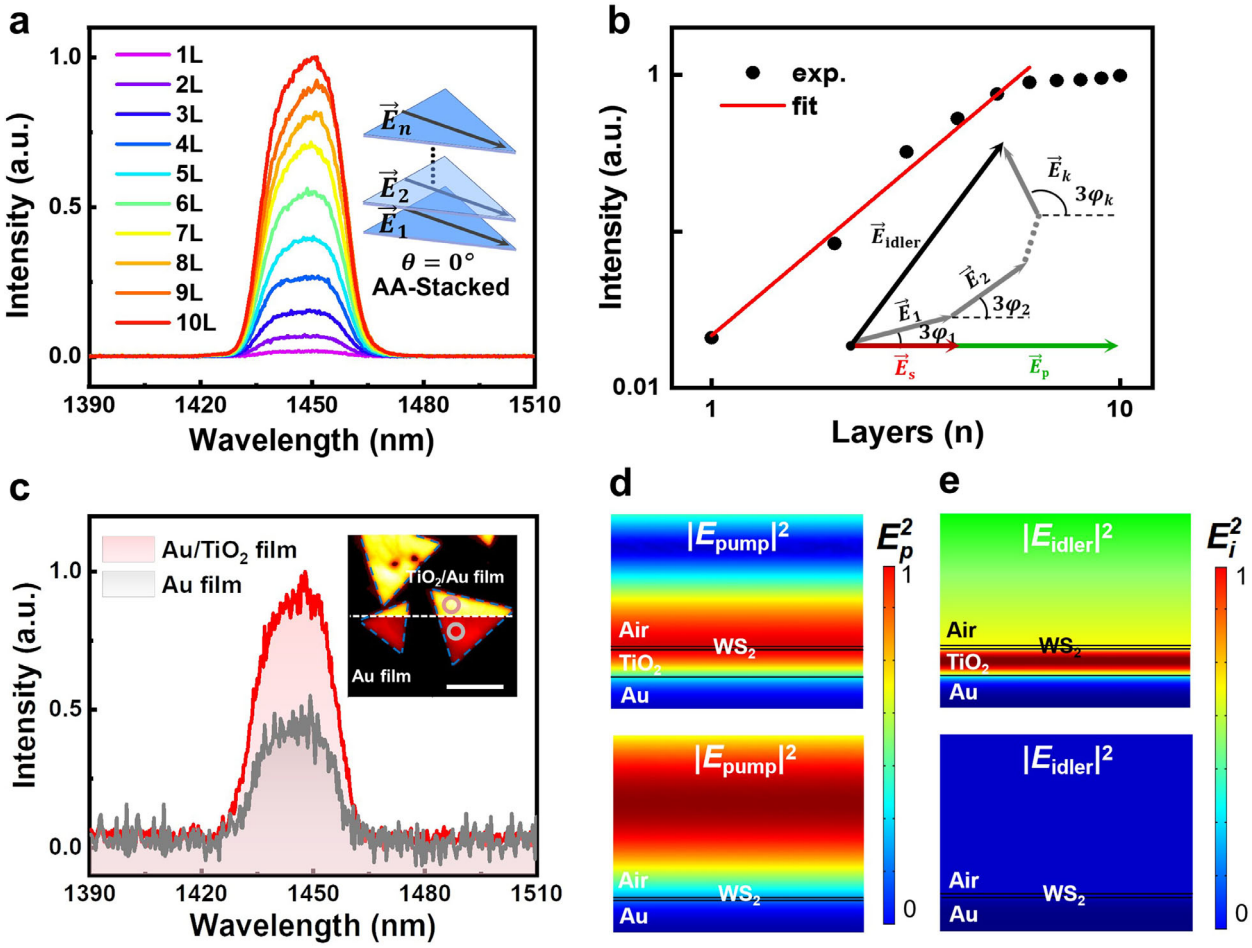

Figure 3. a) Normalized idler spectra under the stacked monolayer WS_2 layers from 1 L to 10 L. Inset: schematics for AA-stacked WS_2 with $\theta = 0°$. b) Extracted idler intensity as a function of the number of layers. Both axes are logarithms. The pump and signal beams are horizontal polarization, and their power is 0.2 and 2 mW, respectively. Inset: a schematic for illustrating the vector superposition of the idler electric fields, where $\vec{E}_p$ and $\vec{E}_s$ are the electric fields of pump and signal, $\vec{E}_k$ is the electric field of idler from the layer k, and $\vec{E}_{idler}$ is the total idler electric field from the stacked region. c) Normalized idler spectra of monolayer WS_2 with TiO_2 film (red line), without TiO_2 film (gray line). Inset: the idler scanning image of monolayer WS_2 with TiO_2 film and without the TiO_2 film. The TiO_2/Au film and Au film areas are separated by a white dashed line. The scale bar is 20 µm. d,e) Calculated distribution patterns of the pump electric-field intensity ($|E_{pump}|^2$) and idler far-field radiation intensity ($|E_{idler}|^2$) in the cross-section of the samples (with TiO_2 film (top) and without TiO_2 film (bottom)).

where $\vec{E}_l$ and $\vec{E}_m$ are the idler electric fields from layer l and m, respectively. $\theta_{lm}=3(\varphi_l - \varphi_m)$ is the stacked angle. Assuming the idler electric field of each layer is the same and the armchairs on each layer are exactly the same direction ($\theta_{lm} = 0$), idler electric field $\vec{E}_k$ yields by each layer can reach a completely coherent superposition.[67] The Equation (3) can be simplified as:[68,69]

$$I_{idler} = n^2 I_k \tag{4}$$

where n is the layer number; I_k is the average idler intensity of the monolayer. Therefore, the use of AA-stacked WS_2 contributes greatly to the enhancement, due to the coherent superposition of the idler field from the individual (see Supplement S1 and Section S9, Supporting Information for more detailed derivation). However, when the layer number exceeds 6, idler intensity increases slowly and reaches saturation in the experiment. For example, the idler intensity of AA-stacked 10 layers of WS_2 is ~62 times than that of the monolayer, which is deviated from the theory value of 100. There could be some reasons. First, as the layer number and the stacked thickness increase, the idler field generated by the top and bottom layers of WS_2 may not effectively form a coherent superposition. Second, the armchair might not be consistent in the transfer process, leading to the polarization angles between the idler from different layers. Third, the bandgap absorption of WS_2 for the pump and the reabsorption for the emitted idler field may also affect the enhancement. Finally, since the influence of the material defect and thermal absorption, the arrangement of atoms in monolayer WS_2 will be slightly disordered or misaligned Therefore, 6 layers of WS_2 are used in our experiment.

As mentioned above, the DFG enhancement comes from the increased local field both at the pump and the signal wavelengths according to Equation (1). Specifically, the F-P mode at pump

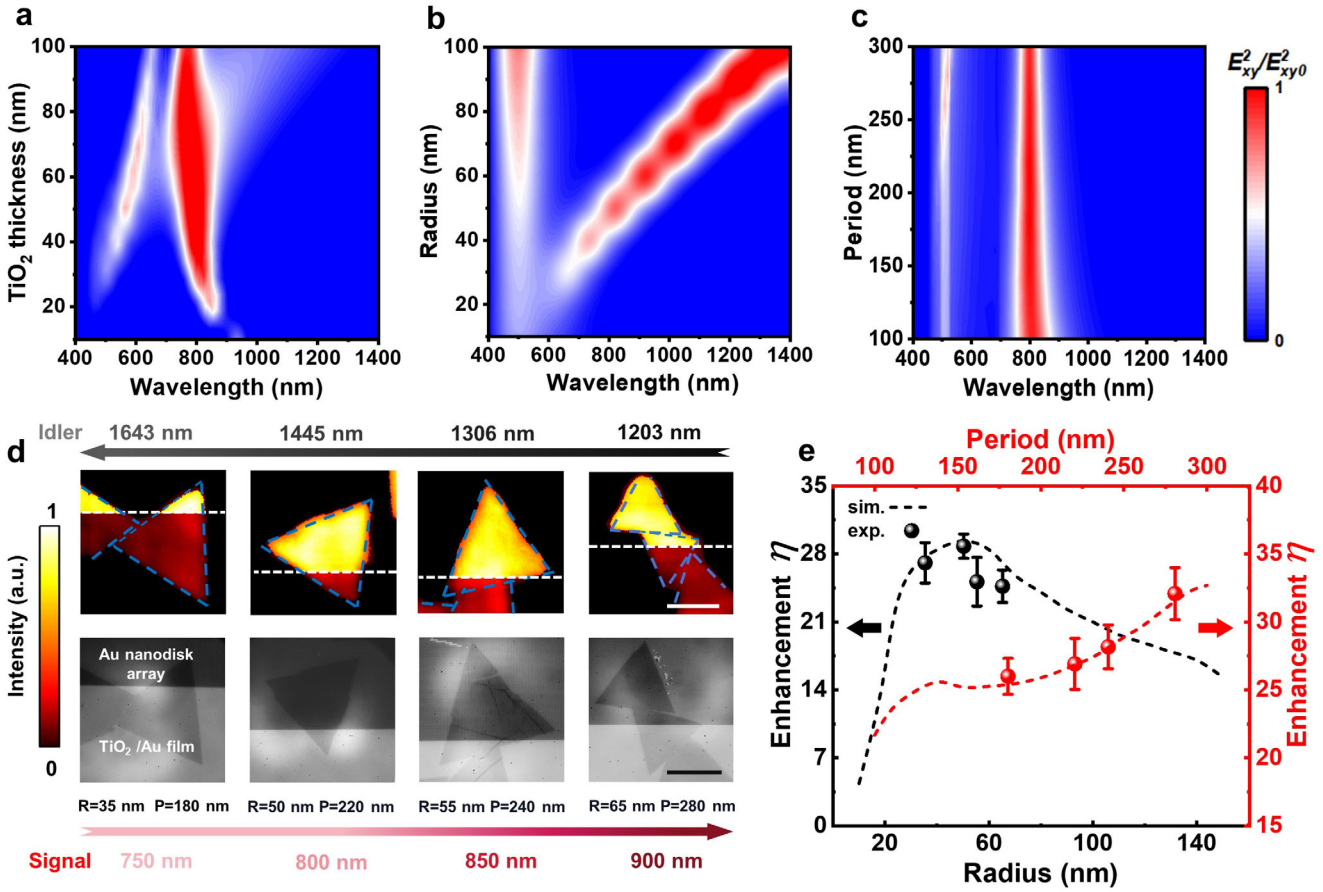

Figure 4. a–c) Calculated the E_{xy}^2/E_{xy0}^2 contour maps as a function of the wavelength and thicknesses of TiO_2 film, Au nanodisk radius, and period. E_{xy}^2 and E_{xy0}^2 represent the average electric field of WS_2 with nanocavity and only on the Au film, respectively. a) Various (λ, T) at $P = 220$ nm, $R = 50$ nm. b) Various (λ, R) at $T = 40$ nm, $P = 220$ nm. c) Various (λ, P) at $T = 40$ nm, $R = 50$ nm. d) Spatial idler mappings of monolayer WS_2 in the nanocavity, and monolayer WS_2 on TiO_2/Au film for different samples of varying R and P (top). The Au nanodisk array and TiO_2/Au film areas are separated by a white dashed line. The same optical microscope images (bottom). Au nanodisk array indicates Au nanodisks on the monolayer WS_2 and TiO_2/Au film, whereas TiO_2/Au film indicates monolayer WS_2 on TiO_2/Au film. Both scale bars are 20 μm. From left to right, the pump wavelength remains 515 nm, and signal wavelengths are 750, 800, 850, and 900 nm, and the idler wavelengths are 1643, 1445, 1306, and 1203 nm, respectively. e) Enhancement factor η as a function of radius (black curve) and period (red curve). The dashed lines depict simulation results, and the dots correspond to the experimental data with error bars.

wavelength possess the strong electric field in WS_2. Because the high refractive index dielectric in the F-P cavity results in a high quality (Q) factor, we choose TiO_2 as the spacer in our experiment.[70] To understand the role of TiO_2, the idler intensity of monolayer WS_2 on TiO_2/Au film (red curve) and on the Au film (gray curve) are experimentally compared for convenience. Figure 3c and the inset show the idler spectra and mapping results. It can be seen clearly that the idler intensity from the monolayer WS_2 on the TiO_2/Au film is stronger than that without TiO_2. We further simulate the average electric-field intensity (E_p^2) at 515 nm in Figure 3d. The pump is reflected on the surface of the Au film and reaches coherent superposition with itself, forming an electric field superposition peak, known as F-P interference. However, when no dielectric on the Au film, the position of WS_2 does not match the strongest electric field region. Thus, TiO_2 film with a thickness of 40 nm is deposited on the Au film, making the WS_2 at the strongest pump intensity (see more details in Supplement S1 and Section S10, Supporting Information). As for the signal wavelength, the electric field intensity (E_s^2) of monolayer WS_2 at 800 nm remains unchanged (see Supplement S1 and Section S11, Supporting Information), due to the mismatch between the signal wavelength and the F-P resonance. To quantitatively calculate the enhancement factor by simulation, Figure 3e shows the idler far-field radiation (E_i^2) at 1445 nm in monolayer WS_2. The simulation demonstrates a 2.87 $\times E_i^2$ enhancement than that without TiO_2, which is similar to the experiment results (2.2×).

Moreover, the influence of TiO_2 thickness on the two modes is explored in simulation. As shown in **Figure 4a**, the resonant frequency of the pump can be tuned (450–650 nm) by varying the TiO_2 thickness, while the resonant wavelength of the signal remains consistent (~800 nm). It indicates the pump-wavelength peak can be tuned independently by varying the TiO_2 thickness. Then the influence of the Au nanodisk radius (R) and period (P) on the resonance wavelength is shown in Figure 4b,c (The

measured absorption spectra of different Au nanodisk arrays are shown in Supplement S1 and Section S12, Supporting Information). To be specific, with increasing the Au nanodisk radius, the signal peak is redshifted from 700 to 1400 nm in Figure 4b, while the pump wavelength holds. Thus, the Au nanodisk radius only influences the LSPR mode, which offers a convenient way for independently tuning the signal wavelength. Thus, the F-P mode and the LSPR mode can be independently tuned by changing the TiO_2 thickness and the Au nanodisk radius. Furthermore, both the resonance wavelengths remain almost unchanged with varied Au nanodisk periods in Figure 4c Note that as the period increases, the coupling between the pump and the nanocavity would lead to an enhancement of the average electric field at the pump.

To reveal the effect of the Au nanodisk on the enhancement experimentally, Figure 4d shows the scanning for four spatial idler mappings, and corresponding optical images of the same region are shown at the bottom. The measured idler spectra are shown in Supplement S1 and Section S13 (Supporting Information). It can be found that every monolayer WS_2 with Au nanodisk array has an obvious enhancement effect on the idler intensity (over 10×) under any parameters than that only on the Au/TiO_2 film. Further, Figure 4e shows the enhancement of the idler intensity with various radii and periods of Au nanodisks. Note that the enhancement factor η is calculated by comparing the extracted idler intensity of the monolayer WS_2 in hybrid nanocavity with that on the Au film for convenience. With increasing the nanodisk radius, η initially increases and then decreases. It is attributed to the attenuation of the LSPR mode at the signal wavelength when the nanodisk radius is less than 20 nm. While the radius exceeds 60 nm, most of the pump beam would be reflected by the nanodisks, leading to a reduction of the local field within the F-P cavity. On the contrary, η monotonically increases with increasing the period. This is the influence of the duty cycle on the pump beam. Furthermore, to quantitatively illustrate the idler enhancement of the hybrid nanocavity, the idler far-field distribution is simulated in Supplement S1 and Section S14 (Supporting Information) (at 1445 nm as an example). The idler far-field radiation from the hybrid nanocavity is 28.1× stronger than that from monolayer WS_2 on the Au film, which is consistent with experiment results (27.6×). Considering the 36× enhancement base on AA-stacked 6 layers WS_2, the total enhancement factor in hybrid nanocavity is calculated to be 1012×, similar to the measured 812× in the experiment. Hence, the dual-resonant nanocavity can enhance the parametric down-conversion in TMDs, offering potential applications in laser systems and mid-infrared sources.

2. Conclusion

In summary, we experimentally demonstrate a dual-resonant nanocavity to achieve a broadband DFG enhancement. The nanocavity consists of AA-stacked WS_2 sandwiched between Au nanodisks and TiO_2/Au film, supporting the F-P mode and LSPR mode in a wide spectral range. The two modes can be respectively tuned to match the wavelengths of the pump at 515 nm and the signal from 750 to 900 nm, which boosts the local electric field at the two excitation wavelengths. Furthermore, the generated idler field is coherently superimposed via AA-stacked WS_2, leading to an additional enhancement. The result shows that over two order-of magnitude idler enhancement is successfully obtained from 1200 to 1650 nm (e.g., 812× at 1445 nm). Moreover, the enhancement effect is independent from the relative angle between the polarization of the pump and the signal. Our work not only provides a new approach for the development of parametric down-conversion of TMDs but also leads the way to ultra-compact frequency converters, on-chip tunable optical parametric amplifiers, and broadens the potential for multifunctional large-scale integration of high-efficiency nonlinear optical devices.

3. Experimental Section

Sample Preparations: The fabrication process of the hybrid nanocavity is illustrated in Supplement S1 and Figure S15 (Supporting Information). First, Au/Cr film with a thickness of 60/10 nm was deposited on a quartz substrate through electron beam evaporation (EBE). Subsequently, 40-nm TiO_2 film was coated on the $Au/Cr/SiO_2$ substrate by magnetron sputtering. Monolayer WS_2 synthesized by the chemical vapor deposition method (6carbon Tech. Shenzhen) was transferred onto the prepared substrate assisted by polydimethylsiloxane (PDMS). For precision fabrication of a high-quality AA-stacked WS_2, each monolayer was transferred to the TiO_2/Au film under the microscope with the help of a home-built motorized transfer stage. Then another monolayer WS_2 was precisely AA stacked on the first monolayer WS_2. During the transfer process, the edges of the triangular profile of each monolayer WS_2 should be kept parallel. Repeat the above operation, high-quality AA-stacked WS_2 will be obtained, which pave the way for the production of Au nanodisk arrays. Finally, the periodic Au nanodisk (100 μm×100 μm) arrays were directly etched and deposited on top of AA-stacked WS_2 using electron beam lithography treatments (EBL, Raith, ELINE Plus) and EBE. The height of the Au nanodisks was fixed at 20 nm, while the array radius and period were varied to acquire different plasmon resonances.

Optical Measurements: As illustrated in Supplement S1 and Figure S16 (Supporting Information), the experiment was performed using a commercial laser system (FLINT, 1030 nm, 76 MHz, full width at half maximum of 120 fs). First, the output beam was divided into two beams by a splitter (THORLABS, VA5-PBS253). One beam was utilized for generating pump pulses at 515 nm through a frequency doubling (AVESTA, ASG-O-800). The other was for generating tunable near-infrared pulses (1320–2000 nm) by Optical Parametric Oscillator (APE, Levante IR OPO), then the pulses were applied for the signal pulses generation within the range of 660 to 1000 nm via SHG (APE, HarmoniXX SHG). Second, the pump and signal pulses remove the fundamental laser with a bandpass filter and a short-pass filter (THORLABS, FBH515-10, and FESH1000). A delay (THORLABS, DDS300/M) was employed to synchronize pump and signal pulses. Third, the pump and signal beams were coherently combined using a dichroic mirror (SEMROCK, Di03-R532-t1-25 × 36) and subsequently focused on the sample through an infrared objective (Mitutoyo-MY50X-825, 50×, 0.42 NA). The approximate half-width of the pump and signal spots is ~1 μm ($D = 2\lambda/\mathrm{NA}\cdot\pi$). Finally, the reflected idler was collected with the same objective to a spectrometer (Andor, Kymera-193i-B1) with an InGaAs CCD (Andor, DU490A-1.7) after a long-pass filter (THORLABS, FELH1100). Optical measurements were carried out at room temperature using a microscope system (Olympus, BX53) configured with a 2D motorized stage (P11.XY100S P11.XY100K, Core Tomorrow).

Supporting Information

Supporting Information is available from the Wiley Online Library or from the author.

Acknowledgements

This work was supported by National Key Research and Development Program of China (No. 2022YFA1604403) and National Natural Science Foundation of China (Nos. 12274157, 12021004, 12274334, and 11904271), and the Natural Science Foundation of Hubei Province of China (2023AFA076, 2022CFB179). Special thanks are given to the Analytical and Testing Center of HUST and the Center of Micro–Fabrication and Characterization (CMFC) of WNLO for the use of their facilities.

Conflict of Interest

The authors declare no conflict of interest.

Author Contributions

C.G. and X.B.H. contributed equally to this work. K.W. and P.X.L. conceived the project. K.W. and P.X.L. supervised the project. C.G. and X.B.H. designed the experiments. C.G. and Y.D.W. performed the experiments. C.G. and Y.D.W. performed theoretical calculations and numerical simulations. C.G., X.B.H., H.L., Y.D.W., L.Y.Z., J.X.Y., S.Z.C., and Z.A.H. analyzed data. All authors discussed the results. C.G., X.B.H., and Y.D.W. drafted the paper with the inputs from all authors.

Data Availability Statement

The data that support the findings of this study are available from the corresponding author upon reasonable request.

Keywords

AA-stacked WS_2, difference frequency generation, Fabry-Perot, localized surface plasmon resonance, transition metal dichalcogenides

Received: November 7, 2024
Revised: February 11, 2025
Published online:

[1] K. Heshami, D. G. England, P. C. Humphreys, P. J. Bustard, V. M. Acosta, J. Nunn, B. J. Sussman, *J. Mod. Opt.* **2016**, *63*, 2005.
[2] B. Öktem, I. Pavlov, S. Ilday, H. Kalaycıoğlu, A. Rybak, S. Yavaş, M. Erdoğan, F. Ö. Ilday, *Nat. Photonics* **2013**, *7*, 897.
[3] C. Xu, F. Wise, *Nat. Photonics* **2013**, *7*, 875.
[4] S. E. Harris, *Proc. IEEE* **1969**, *57*, 2096.
[5] J. A. Black, G. Brodnik, H. Liu, S.-P. Yu, D. R. Carlson, J. Zang, T. C. Briles, S. B. Papp, *Optica* **2022**, *9*, 1183.
[6] Q. Guo, X.-Z. Qi, L. Zhang, M. Gao, S. Hu, W. Zhou, W. Zang, X. Zhao, J. Wang, B. Yan, *Nature* **2023**, *613*, 53.
[7] T. Santiago-Cruz, S. D. Gennaro, O. Mitrofanov, S. Addamane, J. Reno, I. Brener, M. V. Chekhova, *Science* **2022**, *377*, 991.
[8] L. L. Hale, H. Jung, S. D. Gennaro, J. Briscoe, C. T. Harris, T. S. Luk, S. J. Addamane, J. L. Reno, I. Brener, O. Mitrofanov, *ACS Photonics* **2022**, *9*, 1136.
[9] L. Hu, B. Wang, Y. Guo, S. Du, J. Chen, J. Li, C. Gu, L. Wang, *Adv. Opt. Mater.* **2022**, *10*, 2200193.
[10] B. Lounis, M. Orrit, *Rep. Prog. Phys.* **2005**, *68*, 1129.
[11] M. Chekhova, in *Progress in Optics*, *56*, Elsevier, Amsterdam, Netherlands **2011**.
[12] R. Schnabel, *Phys. Rep.* **2017**, *684*, 1.
[13] G. Vallone, E. Pomarico, P. Mataloni, F. De Martini, V. Berardi, *Phys. Rev. Lett.* **2007**, *98*, 180502.
[14] H. J. Briegel, D. E. Browne, W. Dür, R. Raussendorf, M. v. d. Nest, *Nat. Phys.* **2009**, *5*, 19.
[15] M. V. Larsen, X. Guo, C. R. Breum, J. S. Neergaard-Nielsen, U. L. Andersen, *Science* **2019**, *366*, 369.
[16] G. Cerullo, S. De Silvestri, *Rev. Sci. Instrum.* **2003**, *74*, 1.
[17] P. G. Kwiat, K. Mattle, H. Weinfurter, A. Zeilinger, A. V. Sergienko, Y. Shih, *Phys. Rev. Lett.* **1995**, *75*, 4337.
[18] L. Li, Z. Liu, X. Ren, S. Wang, V.-C. Su, M.-K. Chen, C. H. Chu, H. Y. Kuo, B. Liu, W. Zang, *Science* **2020**, *368*, 1487.
[19] Y. Zhang, A. Manjavacas, N. J. Hogan, L. Zhou, C. Ayala-Orozco, L. Dong, J. K. Day, P. Nordlander, N. J. Halas, *Nano Lett.* **2016**, *16*, 3373.
[20] C. C. Wang, G. W. Racette, *Appl. Phys. Lett.* **1965**, *6*, 169.
[21] V. Petrov, *Prog. Quantum Electron.* **2015**, *42*, 1.
[22] A. Fiore, V. Berger, E. Rosencher, P. Bravetti, J. Nagle, *Nature* **1998**, *391*, 463.
[23] C. Manzoni, G. Cerullo, *J. Opt.* **2016**, *18*, 103501.
[24] W. Zhang, H. Yu, H. Wu, P. S. Halasyamani, *Chem. Mater.* **2017**, *29*, 2655.
[25] K. S. Novoselov, A. K. Geim, S. V. Morozov, D.-e. Jiang, Y. Zhang, S. V. Dubonos, I. V. Grigorieva, A. A. Firsov, *Science* **2004**, *306*, 666.
[26] A. Carvalho, M. Wang, X. Zhu, A. S. Rodin, H. Su, A. H. Castro Neto, *Nat. Rev. Mater.* **2016**, *1*, 16061.
[27] X. Wang, Y. Cui, T. Li, M. Lei, J. Li, Z. Wei, *Adv. Opt. Mater.* **2019**, *7*, 1801274.
[28] L. Huang, A. Krasnok, A. Alú, Y. Yu, D. Neshev, A. E. Miroshnichenko, *Rep. Prog. Phys.* **2022**, *85*, 046401.
[29] H. Lin, Y. Song, Y. Huang, D. Kita, S. Deckoff-Jones, K. Wang, L. Li, J. Li, H. Zheng, Z. Luo, *Nat. Photonics* **2017**, *11*, 798.
[30] J. Wu, Y. Yang, Y. Qu, X. Xu, Y. Liang, S. T. Chu, B. E. Little, R. Morandotti, B. Jia, D. J. Moss, *Laser Photonics Rev.* **2019**, *13*, 1900056.
[31] G. Wagoner, P. Persans, E. Van Wagenen, G. Korenowski, *JOSA B* **1998**, *15*, 1017.
[32] H. Zeng, G.-B. Liu, J. Dai, Y. Yan, B. Zhu, R. He, L. Xie, S. Xu, X. Chen, W. Yao, *Sci. Rep.* **2013**, *3*, 1608.
[33] L. M. Malard, T. V. Alencar, A. P. M. Barboza, K. F. Mak, A. M. De Paula, *Phys. Rev. B* **2013**, *87*, 201401.
[34] A. Ciattoni, A. Marini, C. Rizza, C. Conti, *Light Sci. Appl.* **2018**, *7*, 5.
[35] X. Xu, C. Trovatello, F. Mooshammer, Y. Shao, S. Zhang, K. Yao, D. N. Basov, G. Cerullo, P. J. Schuck, *Nat. Photonics* **2022**, *16*, 698.
[36] H. Chen, V. Corboliou, A. S. Solntsev, D.-Y. Choi, M. A. Vincenti, D. De Ceglia, C. De Angelis, Y. Lu, D. N. Neshev, *Light Sci. Appl.* **2017**, *6*, 17060.
[37] H. Hong, C. Wu, Z. Zhao, Y. Zuo, J. Wang, C. Liu, J. Zhang, F. Wang, J. Feng, H. Shen, *Nat. Photonics* **2021**, *15*, 510.
[38] G. Wang, X. Marie, I. Gerber, T. Amand, D. Lagarde, L. Bouet, M. Vidal, A. Balocchi, B. Urbaszek, *Phys. Rev. Lett.* **2015**, *114*, 097403.
[39] Y. Zuo, W. Yu, C. Liu, X. Cheng, R. Qiao, J. Liang, X. Zhou, J. Wang, M. Wu, Y. Zhao, *Nat. Nanotechnol.* **2020**, *15*, 987.
[40] X. Fan, Y. Jiang, X. Zhuang, H. Liu, T. Xu, W. Zheng, P. Fan, H. Li, X. Wu, X. Zhu, *ACS Nano* **2017**, *11*, 4892.
[41] Y. Kim, H. Kim, H. Jang, J.-H. Ahn, J. Lee, *Nano Lett.* **2020**, *20*, 4530.
[42] D. Li, W. Xiong, L. Jiang, Z. Xiao, H. Rabiee Golgir, M. Wang, X. Huang, Y. Zhou, Z. Lin, J. Song, *ACS Nano* **2016**, *10*, 3766.
[43] K. Yao, E. Yanev, H.-J. Chuang, M. R. Rosenberger, X. Xu, T. Darlington, K. M. McCreary, A. T. Hanbicki, K. Watanabe, T. Taniguchi, *ACS Nano* **2019**, *14*, 708.
[44] L. Karvonen, A. Säynätjoki, M. J. Huttunen, A. Autere, B. Amirsolaimani, S. Li, R. A. Norwood, N. Peyghambarian, H. Lipsanen, G. Eda, *Nat. Commun.* **2017**, *8*, 15714.
[45] A. Säynätjoki, L. Karvonen, H. Rostami, A. Autere, S. Mehravar, A. Lombardo, R. A. Norwood, T. Hasan, N. Peyghambarian, H. Lipsanen, *Nat. Commun.* **2017**, *8*, 893.

[46] J. Liang, J. Wang, Z. Zhang, Y. Su, Y. Guo, R. Qiao, P. Song, P. Gao, Y. Zhao, Q. Jiao, *Adv. Mater.* **2019**, *31*, 1808160.
[47] Y. Qu, J. Wu, Y. Yang, Y. Zhang, Y. Liang, H. El Dirani, R. Crochemore, P. Demongodin, C. Sciancalepore, C. Grillet, *Adv. Opt. Mater.* **2020**, *8*, 2001048.
[48] J. Wu, Y. Yang, Y. Qu, L. Jia, Y. Zhang, X. Xu, S. T. Chu, B. E. Little, R. Morandotti, B. Jia, *Small* **2020**, *16*, 1906563.
[49] F. Yi, M. Ren, J. C. Reed, H. Zhu, J. Hou, C. H. Naylor, A. C. Johnson, R. Agarwal, E. Cubukcu, *Nano Lett.* **2016**, *16*, 1631.
[50] J. Shi, X. Wu, K. Wu, S. Zhang, X. Sui, W. Du, S. Yue, Y. Liang, C. Jiang, Z. Wang, *ACS Nano* **2022**, *16*, 13933.
[51] J. Du, J. Shi, C. Li, Q. Shang, X. Liu, Y. Huang, Q. Zhang, *Nano Res.* **2023**, *16*, 4061.
[52] X. Wen, W. Xu, W. Zhao, J. B. Khurgin, Q. Xiong, *Nano Lett.* **2018**, *18*, 1686.
[53] F. Spreyer, C. Ruppert, P. Georgi, T. Zentgraf, *ACS Nano* **2021**, *15*, 16719.
[54] X. Han, K. Wang, P. D. Persaud, X. Xing, W. Liu, H. Long, F. Li, B. Wang, M. R. Singh, P. Lu, *ACS Photonics* **2020**, *7*, 562.
[55] Z. Wang, Z. Dong, H. Zhu, L. Jin, M.-H. Chiu, L.-J. Li, Q.-H. Xu, G. Eda, S. A. Maier, A. T. Wee, *ACS Nano* **2018**, *12*, 1859.
[56] N. Bernhardt, K. Koshelev, S. J. White, K. W. C. Meng, J. E. Froch, S. Kim, T. T. Tran, D.-Y. Choi, Y. Kivshar, A. S. Solntsev, *Nano Lett.* **2020**, *20*, 5309.
[57] Z. Liu, J. Wang, B. Chen, Y. Wei, W. Liu, J. Liu, *Nano Lett.* **2021**, *21*, 7405.
[58] C. Li, X. Lu, A. Srivastava, S. D. Storm, R. Gelfand, M. Pelton, M. Sukharev, H. Harutyunyan, *Nano Lett.* **2020**, *21*, 1599.
[59] T. Zhang, Q. Guo, Z. Shi, S. Zhang, H. Xu, *ACS Photonics* **2023**, *10*, 1529.
[60] Y. Wang, M. Ghotbi, S. Das, Y. Dai, S. Li, X. Hu, X. Gan, J. Zhao, Z. Sun, *Nanoscale* **2020**, *12*, 19638.
[61] C. Trovatello, A. Marini, X. Xu, C. Lee, F. Liu, N. Curreli, C. Manzoni, S. Dal Conte, K. Yao, A. Ciattoni, *Nat. Photonics* **2021**, *15*, 6.
[62] J. Zhao, A. Fieramosca, R. Bao, W. Du, K. Dini, R. Su, J. Feng, Y. Luo, D. Sanvitto, T. C. Liew, *Nat. Nanotechnol.* **2022**, *17*, 396.
[63] Q. Yang, W. Jiayang, Z. Yuning, Y. Yunyi, J. Linnan, D. Houssein El, K. Sébastien, S. Corrado, D. Pierre, G. Christian, M. Christelle, J. Baohua, D. J. Moss, *Light: Adv. Manuf.* **2024**, *4*, 452.
[64] C. Janisch, Y. Wang, D. Ma, N. Mehta, A. L. Elías, N. Perea-López, M. Terrones, V. Crespi, Z. Liu, *Sci. Rep.* **2014**, *4*, 5530.
[65] Y.-R. Shen, *The principles of nonlinear optics*, John Wiley & Sons, New York, **1984**.
[66] W. Hsu, Z. Zhao, L. Li, C. Chen, M. Chiu, P. Chang, Y. Chou, W. Chang, *ACS Nano* **2014**, *8*, 2951.
[67] J. He, K. Hummer, C. Franchini, *Phys. Rev. B* **2014**, *89*, 075409.
[68] F. Liu, W. Wu, Y. Bai, S. H. Chae, Q. Li, J. Wang, J. Hone, X.-Y. Zhu, *Science* **2020**, *367*, 903.
[69] M. Zhao, Z. Ye, R. Suzuki, Y. Ye, H. Zhu, J. Xiao, Y. Wang, Y. Iwasa, X. Zhang, *Light Sci. Appl.* **2016**, *5*, 16131.
[70] H. Y. Jeong, U. J. Kim, H. Kim, G. H. Han, H. Lee, M. S. Kim, Y. Jin, T. H. Ly, S. Y. Lee, Y.-G. Roh, *ACS Nano* **2016**, *10*, 8192.